*J. Fluid Mech.* (2018), *vol.* 837, *pp.* 627–639. © Cambridge University Press 2018 
doi:10.1017/jfm.2017.886

# Longitudinal development of flow-separation lines on slender bodies in translation

**S.-K. Lee**[1,2,†]

[1]Defence Science and Technology Group, Melbourne, VIC 3207, Australia

[2]Australian Maritime College, University of Tasmania, Launceston, TAS 7250, Australia

(Received 5 July 2017; revised 13 November 2017; accepted 30 November 2017; first published online 5 January 2018)

This paper examines flow-separation lines on axisymmetric bodies with tapered tails, where the separating flow takes into account the effect of local body radius $r(x)$, incidence angle $\psi$ and the body-length Reynolds number $Re_L$. The flow is interpreted as a transient problem which relates the longitudinal distance $x$ to time $t^* = x\tan(\psi)/r(x)$, similar to the approach of Jeans & Holloway (*J. Aircraft*, vol. 47 (6), 2010, pp. 2177–2183) on scaling separation lines. The windward and leeward sides correspond to the body azimuth angles $\Theta = 0$ and 180°, respectively. From China-clay flow visualisation on axisymmetric bodies and from a literature review of slender-body flows, the present study shows three findings. (i) The time scale $t^*$ provides a collapse of the separation-line data, $\Theta$, for incidence angles between 6 and 35°, where the data fall on a power law $\Theta \sim (t^*)^k$. (ii) The data suggest that the separation rate $k$ is independent of the Reynolds number over the range $2.1 \times 10^6 \leqslant Re_L \leqslant 23 \times 10^6$; for a primary separation $k_1 \simeq -0.190$, and for a secondary separation $k_2 \simeq 0.045$. (iii) The power-law curve fits trace the primary and secondary lines to a characteristic start time $t_s^* \simeq 1.5$.

**Key words:** aerodynamics, separated flows, wakes/jets

## 1. Introduction

A slender body at incidence to a moving stream experiences a lift force, where this force is largely influenced by cross-flow separation in the form of wake vortices. There is a wealth of research literature on studies of inclined slender-body wakes given their relevance, for example, in the dynamic control and prediction of safe manoeuvre of airships and submarines. Some useful references to supplement reading include the works of Sarpkaya (1966) and Schindel (1969) on vortex separation about lifting bodies, the measurement techniques discussed by Wetzel (1996) and Chesnakas & Simpson (1997) for detecting surface-flow separation lines, the use of topological concepts by Wang (1972), Tobak & Peake (1982) and Lee (2015) to interpret cross-flow patterns and the use of high-resolution Reynolds-averaged Navier–Stokes computation by Jeans *et al.* (2009) to obtain vorticity fields for force estimation. An insight into slender-body wakes also may be found in more recent literature. Examples include the high-Reynolds-number experiments by Ashok, Van Buren & Smits (2015) which documented the persistence of natural asymmetry in

† Email address for correspondence: soon-kong.lee@dst.defence.gov.au

https://doi.org/10.1017/jfm.2017.886 Published online by Cambridge University Press

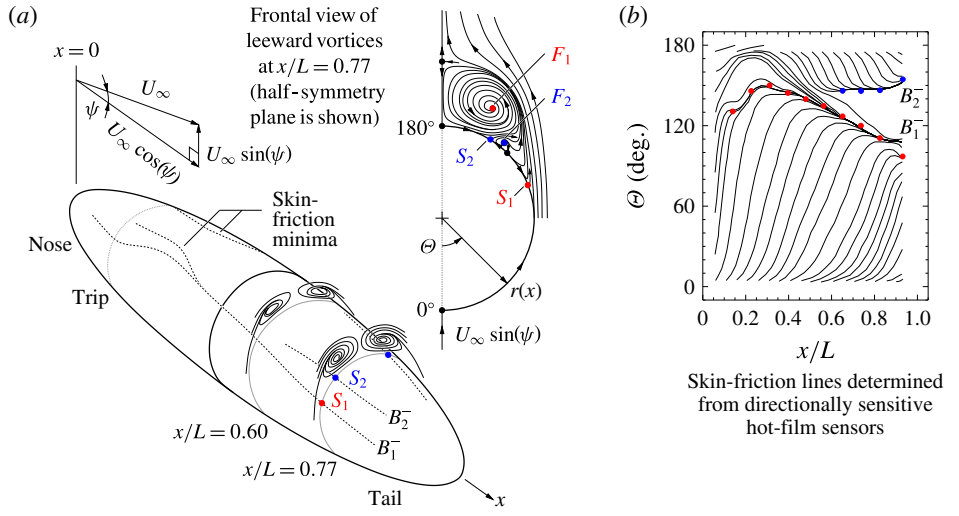


FIGURE 1. (Colour online) Flow separation over a slender body (6:1 prolate spheroid at $\psi = 20°$); the body-length Reynolds number $Re_L$ is (*a*) $4.2 \times 10^6$ and (*b*) $6.5 \times 10^6$. After Wetzel, Simpson & Chesnakas (1998).

wake vortices, and the direct numerical simulation of Jiang *et al.* (2016) which presented data for testing of concepts of self-similarity in asymmetric wakes, where the wakes may be dominated by complex helical-like vortices.

It is interesting, from laboratory observation and from the literature review, that the most apparent features of slender-body wakes are the surface-flow separation lines because these lines define the start of the wakes. An example of a slender body which has been extensively tested is that of a prolate spheroid (e.g. Chesnakas & Simpson 1997; Wetzel *et al.* 1998). In figure 1(*a*), the cross-flow pattern constructed from laser-Doppler-velocimetry data and the skin-friction minima obtained from hot-film data show the separation lines (or negative surface bifurcations $B_1^-$ and $B_2^-$) on this geometry, where these lines correspond to saddle points ($S_1$ and $S_2$) of the wake flow. A detailed map of the skin-friction lines is given in figure 1(*b*), where the locations of separations are identified by the local minima of skin-friction magnitude (see Wetzel *et al.* 1998). Here, the wake flow contains a pair of counter-rotating primary and secondary vortices. In the half-symmetry plane shown in figure 1, the larger vortex is a sink focus ($F_1$) produced by the primary separation ($B_1^-$), and the smaller eddy is a source focus ($F_2$) adjacent to the secondary separation ($B_2^-$) to satisfy flow continuity. Since the wake flow starts from the separation lines, the off-body vortices generally move in the same longitudinal direction as the separation lines.

Figure 2(*a*) provides a schematic diagram of a generic slender body which consists of a rounded nose of length $l_n$, a cylindrical midsection of length $l_m$ and a tapered tail of length $l_t$. In the case of a prolate spheroid (e.g. figure 1), the nose and the tail are mirrored geometries of equal length ($l_n = l_t$) and there is no cylindrical midsection.

For translational motion as shown in figure 2(*b*), Jeans & Holloway (2010) indicated that the development of separation lines over the body at incidence $\psi$ may be formulated as a transient problem which relates the longitudinal distance ($x$ measured from the nose) to time:

$$t = \frac{x}{U_\infty \cos(\psi)}, \quad t^*_{r_m} = t\,\frac{U_\infty \sin(\psi)}{r_m} = \frac{x}{r_m}\tan(\psi), \qquad (1.1a,b)$$

https://doi.org/10.1017/jfm.2017.886 Published online by Cambridge University Press

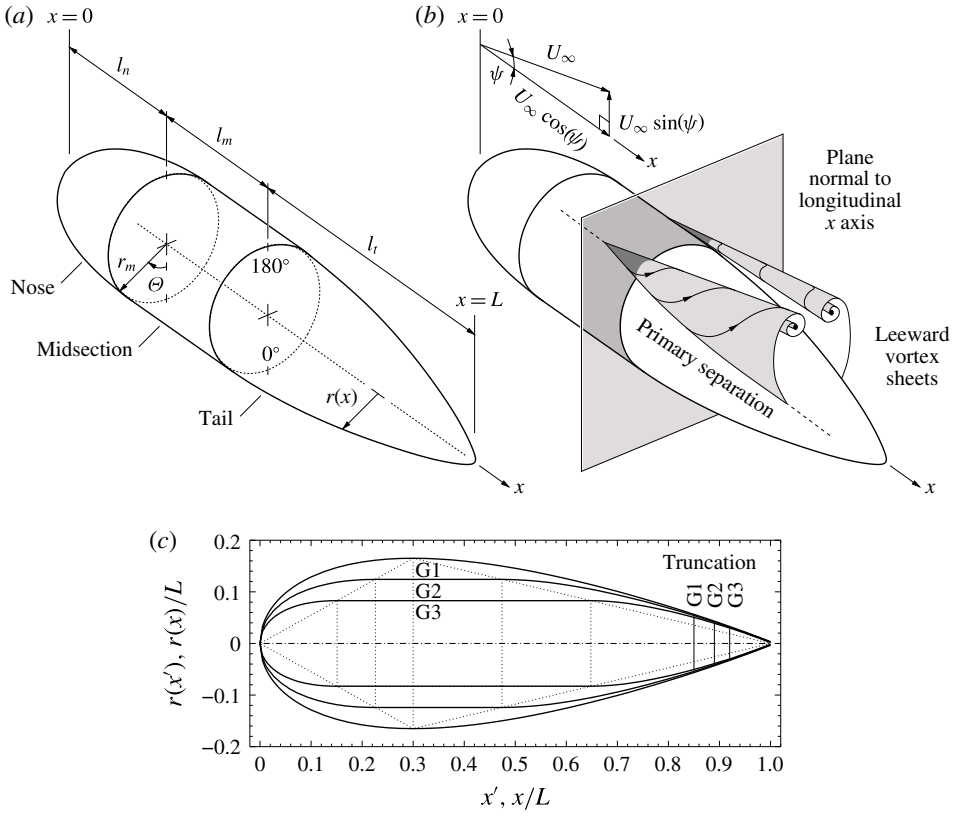


FIGURE 2. Schematic diagram of a generic slender body: (*a*) component definitions and (*b*) cross-flow orientation. Dimensions for (*c*) test geometries G1, G2 and G3 are given in table 1.

where $r_m$ is the maximum radius of the body, and $\tan(\psi)$ defines the ratio between the cross-flow and body-axis components of the free-stream velocity $U_\infty$. The scaling (1.1) is based on an analogy by Sarpkaya (1966) and Schindel (1969) which relates the development of cross-flow at each longitudinal station along the slender body to the development with time of the flow on an impulsively started two-dimensional cylinder. This analogy is derived from a National Advisory Committee for Aeronautics (NACA) vortex model described by Allen (1949), among others, for predicting lift.

In their study, Jeans & Holloway (2010) developed a model to scale the primary-separation angle ($\Theta_{B_1^-}$) as a function of $t^*_{r_m}$, the non-dimensionalised time defined in (1.1), for a collection of different submarine hull forms with the aid of a Reynolds-averaged Navier–Stokes (RANS) simulation database. Their findings indicated that the length (or time) of the primary separation increases with the incidence angle $\psi$, and that $\psi$ has a strong effect on the separation lines along the tapered tail (see component definitions in figure 2). Upstream of the tail, Jeans & Holloway (2010) observed that the primary-separation angle along the cylindrical midsection of a slender body approximately follows the exponential function:

$$(\Theta_{B_1^-} - \Theta^\infty_{B_1^-})/(\Theta^o_{B_1^-} - \Theta^\infty_{B_1^-}) \simeq \mathrm{e}^{-k_{r_m}\, t^*_{r_m}}, \tag{1.2}$$

https://doi.org/10.1017/jfm.2017.886 Published online by Cambridge University Press

| Geometry | Fineness ratio $R = L/(2r_m)$ | Nose length $l_n/L$ | Midsection length $M = l_m/(2r_m)$ | $l_m/L$ | Tail length $l_t/L$ | Sting entry $x_s/L$ |
|---|---|---|---|---|---|---|
| G1 | 3.0 | 0.30 | 0 | 0 | 0.70 | 0.85 |
| G2 | 4.0 | 0.23 | 1 | 0.25 | 0.52 | 0.89 |
| G3 | 6.0 | 0.15 | 3 | 0.50 | 0.35 | 0.92 |

TABLE 1. Test geometries with body length $L = l_n + l_m + l_t$ and maximum radius $r_m$ as shown in figure 2.

where $\Theta^o_{B_1^-} = 180^\circ$ is chosen to correspond to the leeward side, and the steady-state separation angle $\Theta^\infty_{B_1^-} \simeq 112^\circ$ and the exponent $k_{r_m} \simeq 0.5$ are obtained empirically since it is difficult to determine exactly where separation first occurs. This is mainly because there are no sharp edges to fix the separation, and where separation first occurs it is likely dependent on the initial development over the slender body.

The aim of the work reported in the following pages is to obtain further understanding of the development of flow-separation lines on inclined slender bodies. The key parameters of interest include the body geometry and the incidence angle. Here, the separation lines are interpreted by using flow-visualisation data from present wind-tunnel experiments and by using high-Reynolds-number data from open literature.

## 2. Body geometry and experimental technique

This study makes use of an existing generic axisymmetric body which is available from the Aerospace Division of the Defence Science and Technology Group. The slender body of choice has a NACA0033 profile with the fineness ratio $R = L/(2r_m)$, where the nose and the tail can be split at the location of maximum radius $r_m$ so that a cylindrical midsection (of radius $r_m$) can be introduced to increase the overall body length $L$. Figure 2(*c*) shows the geometry with three different lengths $l_m$ of the midsection: $M = l_m/(2r_m) = 0$, 1 and 3. For $M = 0$, this defines the NACA geometry with length $x/L \equiv x'$ in the range $0 \leqslant x' \leqslant 1$ and the local body radius $r(x)/L \equiv r(x')$, where

$$r(x') = 0.33(1.4845\sqrt{x'} - 0.6300x' - 1.7580(x')^2 + 1.4215(x')^3 - 0.5075(x')^4). \quad (2.1)$$

For $M > 0$, the details of the nose, the midsection and the tail are given below and in table 1.

(i) The NACA nose has the profile

$$\left.\frac{x}{L}\right|_n = \frac{x'}{0.33M + 1}, \quad \left.\frac{r(x)}{L}\right|_n = \frac{r(x')}{0.33M + 1}, \quad \frac{l_n}{L} = \frac{0.3}{0.33M + 1}, \quad (2.2a\text{–}c)$$

with $0 \leqslant x' \leqslant 0.3$ and $0 \leqslant x \leqslant l_n$, where $l_n$ is the length of the nose.

(ii) The cylindrical midsection has the proportions

$$\left.\frac{r(x)}{L}\right|_m = \frac{r_m}{L} = \frac{0.33/2}{0.33M + 1}, \quad \frac{l_m}{L} = \frac{0.33M}{0.33M + 1}, \quad (2.3a,b)$$

with $l_n < x \leqslant l_n + l_m$, where $l_m$ is the length of the midsection.

https://doi.org/10.1017/jfm.2017.886 Published online by Cambridge University Press

(iii) The NACA tail has the profile

$$\left.\frac{x}{L}\right|_t = \frac{0.33M + x'}{0.33M + 1}, \quad \left.\frac{r(x)}{L}\right|_t = \frac{r(x')}{0.33M + 1}, \quad \frac{l_t}{L} = \frac{L - (l_n + l_m)}{L} = \frac{0.7}{0.33M + 1}, \tag{2.4a–c}$$

with $0.3 < x' \leqslant 1$ and $l_n + l_m < x \leqslant l_n + l_m + l_t$, where $l_t$ is the length of the tail. To allow sting mounting for wind-tunnel testing, the tail is truncated at the longitudinal location (see table 1):

$$\frac{x_s}{L} = \frac{0.33M + 0.85}{0.33M + 1}. \tag{2.5}$$

The slender body has a fixed maximum radius $r_m = 64$ mm; it is made of aluminium and is painted black for testing in the DST low-speed wind tunnel. The wind-tunnel test section has width 2.7 m, height 2.1 m and length 6.6 m (e.g. Erm 2003). The free stream is operated at $U_\infty = 85$ m s$^{-1}$, 64 m s$^{-1}$ and 42 m s$^{-1}$ for the respective geometries G1, G2 and G3 to yield the same body-length Reynolds number $Re_L = LU_\infty/\nu = 2.1 \times 10^6$, where $\nu$ is the kinematic viscosity of the working fluid (i.e. air). To trip the flow, a circumferential ring of fine carborundum particles (of size 100 μm) is fixed at 15 % of the body length $L$.

The body is attached to a sting and is remote controlled by a sting-column rig which allows pitch ($0° \leqslant \psi < 40°$), roll and vertical traverse. To visualise the surface flow, a paint mixture of white China-clay powder (∼9 % by volume), kerosene (∼90 %) and oleic acid (∼1 %) is used for this experiment. Trial and error indicated that the best results are obtained by painting the body just outside the test section (above a rectangular open slot in the test-section ceiling) and immediately traversing the body down to a set point in the test section at the required pitch while the wind tunnel is running at the correct flow speed. This process helps to avoid spurious flow patterns produced by (i) the initial ramp-up of the tunnel speed, and (ii) the gravitational effect on the paint mixture.

Once the flow pattern has settled with the kerosene evaporated (which takes a few minutes), the dried China clay provides a strong contrast against the black body to allow still photography. A 360° view is obtained with a fixed position of the camera as the rig rolls the body about its longitudinal axis. Images of the flow pattern are recorded for each pitch or incidence angle $\psi = 20$, 25, 30 and 35°. The present test omitted angles $\psi \leqslant 15°$ because the separation lines at these angles occur much further aft and are affected by flow stagnation at the sting junction; also they are more difficult to measure due to smaller spatial dimension of the tapered tail.

## 3. Flow topology of the slender body

Figure 3 shows examples of recorded China-clay images for the geometry G1. The other geometries G2 and G3 produce very similar surface-flow patterns. The major features (as shown in figure 3) are interpreted as follows.

(i) The source node $N_1$ – this is due to flow stagnation on the windward side of the nose.

(ii) The positive bifurcations $B_1^+$ and $B_2^+$ – they define on the slender body the bottom and top symmetry lines which extend from the source node to the truncated tail.

(iii) The negative bifurcations $B_1^-$ and $B_2^-$ – they represent regions of concentrated surface streaklines. The flow spreading circumferentially from the bottom

https://doi.org/10.1017/jfm.2017.886 Published online by Cambridge University Press

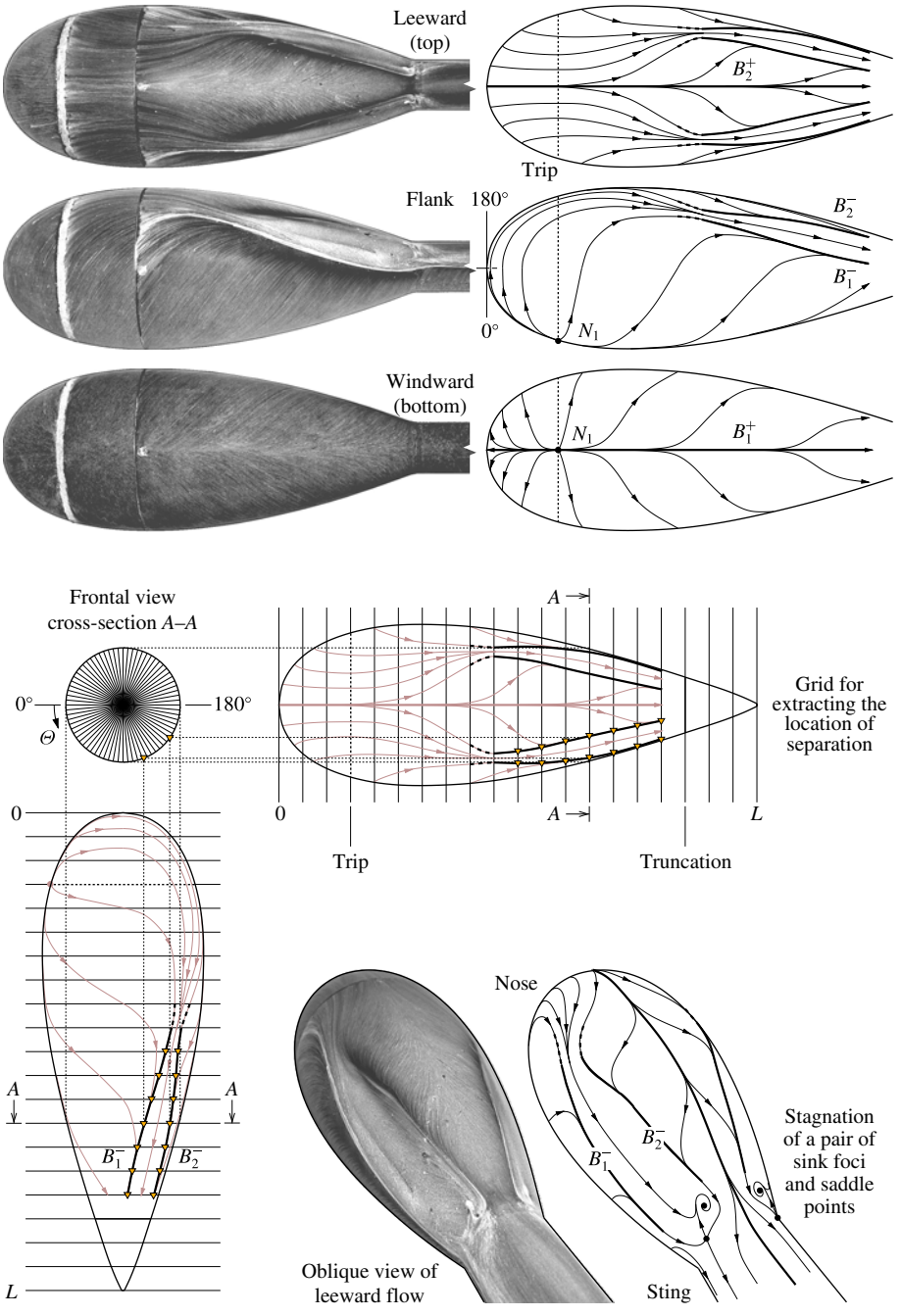


FIGURE 3. (Colour online) China-clay images and surface streaklines for geometry G1; $\psi = 35°$; $Re_L = 2.1 \times 10^6$.

(windward side; $\Theta = 0°$) and the top (leeward side; $\Theta = 180°$) of the body converges here to satisfy flow continuity. The negative bifurcation closest to the windward side is the primary line ($\Theta_{B_1^-}$) and the negative bifurcation closest to

https://doi.org/10.1017/jfm.2017.886 Published online by Cambridge University Press

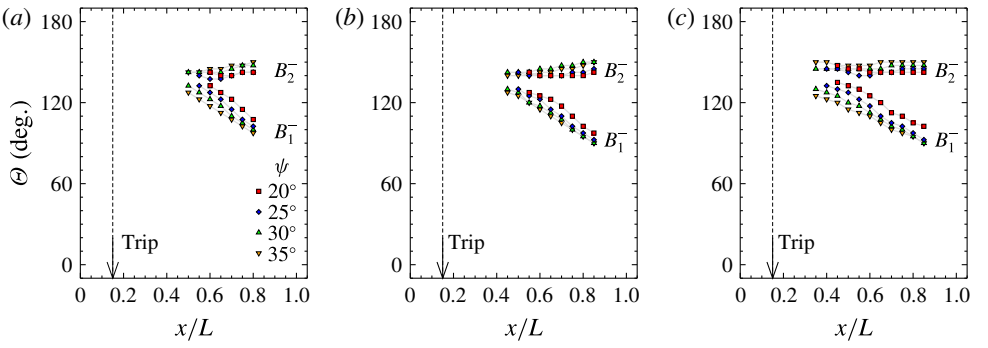


FIGURE 4. (Colour online) Separation lines on geometries (*a*) G1, (*b*) G2 and (*c*) G3; $Re_L = 2.1 \times 10^6$.

the leeward side is the secondary line ($\Theta_{B_2^-}$). The separation angles fall in the range $0° < \Theta_{B_1^-} < \Theta_{B_2^-} < 180°$.

In figure 3, the surface streaklines are visually traced from the China-clay images (using the 'Xfig' graphics software) to identify the separation locations. To obtain discrete measurements from each geometry, the streakline pattern is divided into 20 longitudinal segments at increments $x/L = 0.05$ with 72 azimuthal segments at increments $\Theta = 5°$ and assigning the locations of the separations ($\Theta_{B_1^-}$ and $\Theta_{B_2^-}$) to the nearest segments. The size of the selected grid in the azimuthal $\Theta$ direction is the approximate minimum in which the separation locations can be resolved visually (with a measurement uncertainty $\delta_\Theta \simeq \pm 5°$). For each geometry at a given incidence angle, the pattern is folded about the symmetry plane to reduce possible scatter, and the results are summarised as a collection of discrete data points in figure 4.

Given that the slender body is truncated to blend into a cylindrical sting, figure 3 shows that the separation lines can stagnate at this junction and terminate as a pair of sink foci and saddle points. In figure 4, the measurements are taken sufficiently upstream of the truncation to avoid possible effect of stagnation due to the sting–body junction. If the slender body is not truncated and if there is no sting interference, then the simplest possible flow pattern is that which all streaklines originate from a source node on the nose and eventually terminate at a sink node on the tail to satisfy the closed-surface topology, that is, number of nodes − number of saddles = 2 (e.g. Wang 1972; Tobak & Peake 1982; Lee 2015).

## 4. Separation lines of the surface flow

Inspection of the flow topology in figure 3 and dimensional analysis of the data in figure 4 suggest that the azimuthal location of separation, $\Theta$, may be expressed as a function of longitudinal development time and the body-length Reynolds number,

$$\Theta = \boldsymbol{f}(t^*, Re_L), \tag{4.1}$$

where $t^*$ is a generalised form of the time scale (1.1) which relates to the local body radius $r(x)$ and the incidence angle $\psi$, *viz.*

$$t^* = t^*_{r_m} \frac{r_m}{r(x)} = \frac{x}{r(x)} \tan(\psi). \tag{4.2}$$

https://doi.org/10.1017/jfm.2017.886 Published online by Cambridge University Press

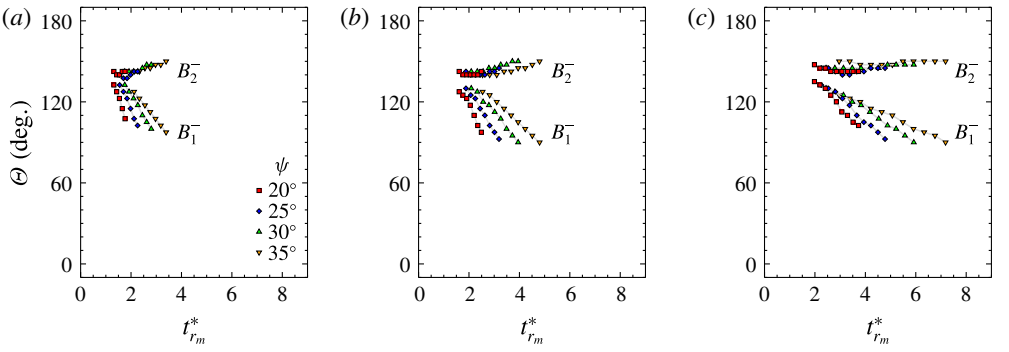


FIGURE 5. (Colour online) Separation lines as functions of $t^*_{r_m}$ for (*a*) G1, (*b*) G2 and (*c*) G3; $Re_L = 2.1 \times 10^6$.

### 4.1. *On the time scale*

A plot of the data from figure 4 as a function of (1.1) in figure 5 shows the effect of the tapered tail on the flow separation, where an increase in $\psi$ increases the characteristic time $t^*_{r_m}$ of the separation lines. To account for the different trends in separation along the tail, the data points are replotted in figure 6, where $t^*_{r_m}$ is weighted by the ratio $r_m/r(x)$ as defined in (4.2). Figure 6 shows that the $t^*$ scaling yields a collapse of all the data points; a slight scatter may be due to (i) the uncertainty in the visual inspection $\delta_\theta \simeq \pm 5°$, and/or (ii) the strong turbulence of the separating flow since the splitting of the NACA geometry (G1) to include a long cylindrical midsection (G2, G3) makes the geometry less streamlined.

Inspection of figure 6 suggests that the locus of separation ($l$) may be approximated by a power law of $t^*$, *viz.*

$$\Theta_{B_l^-} \sim (t^*)^{k_l}, \quad t^* \geqslant t^*_s, \quad l = 1, 2, \tag{4.3}$$

where $t^*_s$ is the start time for the power law and $k$ is the separation rate. Given that there is little discernible difference between the separation trends in figure 6, the data points for geometries G1, G2 and G3 are combined in figure 7(*a*) to provide an estimate of $k$. In figure 7(*a*), the root-mean-square (r.m.s.) difference between the power law and the combined data for the primary line is 3.5 % with $k_1 = -0.223$, and for the secondary line the r.m.s. difference is 1.8 % with $k_2 = 0.033$. For the power-law curve fits shown in figure 7(*a*), the start time is at $t^*_s = 1.42$.

### 4.2. *On the Reynolds number*

In figure 7(*a*), the time scale $t^*$ provides a collapse of all the data points for the different geometries (G1, G2 and G3) tested in the range $20° \leqslant \psi \leqslant 35°$ at a fixed body-length Reynolds number $Re_L = 2.1 \times 10^6$. The collapsed data are well represented by a power law, $\Theta \sim (t^*)^k$, and so the exponent $k$ can be used as a measure of separation rate.

To investigate the effect of increasing body-length Reynolds number ($Re_L$) on the separation rate $k$ defined by (4.3), a larger slender body of fineness ratio $R = 10.0$ has been constructed for testing in the DST low-speed wind tunnel. This 2 metre long body consists of an axisymmetric (NACA0018) nose and a cylindrical section of fixed radius ($r_m$ = 100 mm) without a tapered tail. Figure 7(*b*) summarises the

https://doi.org/10.1017/jfm.2017.886 Published online by Cambridge University Press

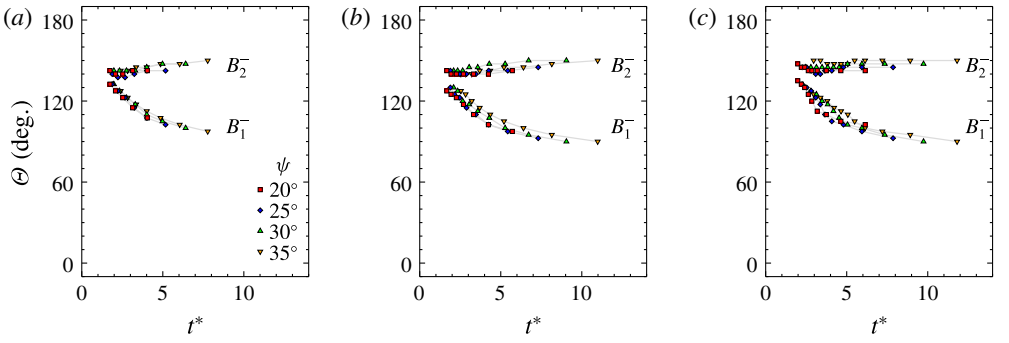


FIGURE 6. (Colour online) Separation lines as functions of $t^*$ for (*a*) G1, (*b*) G2 and (*c*) G3; $Re_L = 2.1 \times 10^6$.

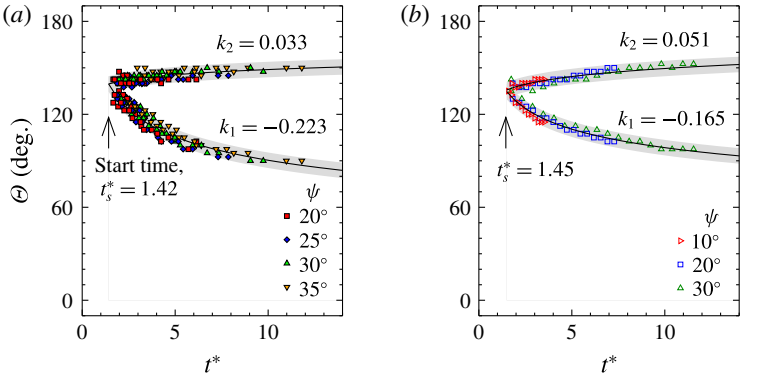


FIGURE 7. (Colour online) Present study of separation lines on slender bodies. (*a*) All data points taken from figure 6; $Re_L = 2.1 \times 10^6$. (*b*) Supplementary China-clay data from a NACA0018-nose-cylinder; $Re_L = 8 \times 10^6$. The solid curves show the separations modelled by (4.3) with a $\pm 5°$ departure indicated by the shaded regions.

separation-line data for this geometry over a range of incidence angles at $Re_L = 8 \times 10^6$ (flow speed of 60 m s$^{-1}$). The collapse of the data in figure 7(*b*) indicates that $t^*$ is a suitable scaling for a slender body without a tapered tail.

To assist interpretation, the present study is supplemented by high-Reynolds-number data taken from open literature, where the review data for $\Theta$ are presented here as a function of time $t^*$. Examples are given in figure 8 for generic axisymmetric hull forms tested in the range $11.7 \times 10^6 \leqslant Re_L \leqslant 23 \times 10^6$ by Jeans & Holloway (2010), and in figure 9 for a 6:1 prolate spheroid tested at $Re_L = 4.2 \times 10^6$ and $6.5 \times 10^6$ by Wetzel (1996) and co-workers.

In their RANS study of separating flow from submarine hulls, Jeans & Holloway (2010) reported only the primary-separation lines determined from the local minima of skin-friction distributions. Details of the submarine hulls are available in Van Randwijck & Feldman (2000) for the 'Series 58 model 4621', in Groves, Huang & Chang (1989) for the 'DARPA SUBOFF' and in Mackay (2003) for the 'DRDC STR', where the hull profiles are used to calculate the time scale $t^*$ as defined in (4.2). For clarity, figure 8 plots the data with and without vertical offsets to show the collapse of the data for the different hull forms.

https://doi.org/10.1017/jfm.2017.886 Published online by Cambridge University Press

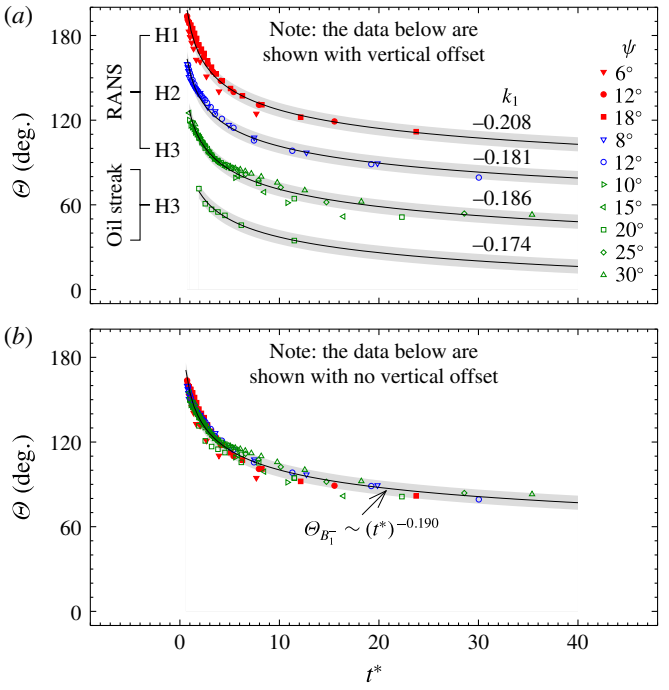


FIGURE 8. (Colour online) Generic submarine hull forms: the data points are shown (*a*) with and (*b*) without vertical offset. (H1) Series 58 model 4621 for $Re_L = 11.7 \times 10^6$, (H2) DARPA SUBOFF for $Re_L = 14 \times 10^6$ and (H3) DRDC STR for $Re_L = 23 \times 10^6$ calculated from the RANS and oil streak data of Jeans & Holloway (2010). H1 data points are offset by $(\Delta t^*, \Delta\Theta) = (0, 30°)$, H2 data points are offset by (0, 0°), H3 RANS data points are offset by (0, −30°) and H3 oil streak data points are offset by (0, −60°). The curves are modelled by (4.3) with a ±5° departure indicated by the shaded regions.

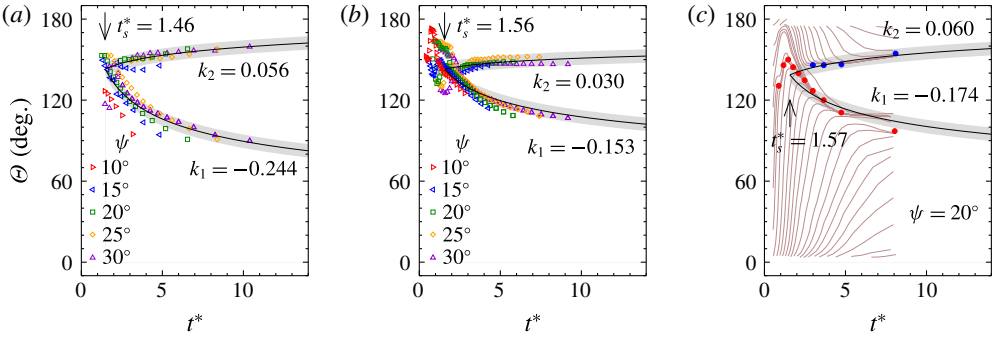


FIGURE 9. (Colour online) Flow separation on a 6:1 prolate spheroid calculated from wind-tunnel data (Wetzel 1996; Wetzel *et al.* 1998). (*a*) Oil flow; $Re_L = 4.2 \times 10^6$. (*b*) Directionally sensitive hot-films (constant current) at $Re_L = 4.2 \times 10^6$ and (*c*) $6.5 \times 10^6$; also see figure 1(*b*). The curves are modelled by (4.3) with a ±5° departure indicated by the shaded regions.

For Wetzel (1996), the primary and secondary lines on the 6:1 prolate spheroid are determined by streaklines from oil flow visualisation and by skin-friction vectors via

https://doi.org/10.1017/jfm.2017.886 Published online by Cambridge University Press

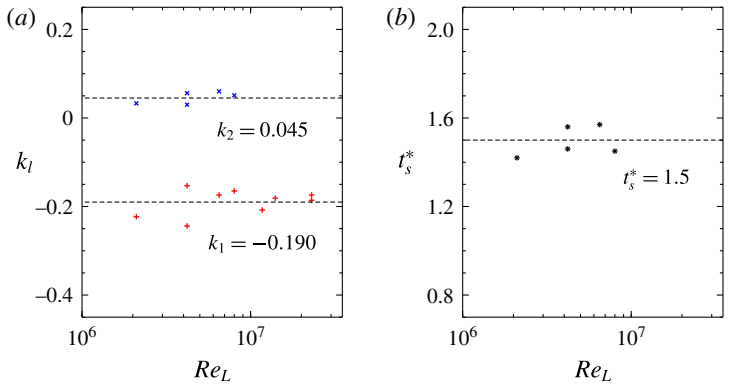


FIGURE 10. (Colour online) (*a*) Power-law (4.3) exponent $k_l$ (primary line $l=1$; secondary line $l=2$) and (*b*) start time $t_s^*$ as functions of the body-length Reynolds number $Re_L$ taken from figures 7–9.

directionally sensitive hot-films. In figure 9(*a*), the large scatter of the oil flow data is likely due to gravity, where the effect is more apparent for the weaker separations at smaller angles of $\psi$. Unlike the oil flow, the hot-film technique adopted by Wetzel has no inherent bias (also see Wetzel *et al.* 1998) and figure 9(*b*) shows that the measurements in the range $10^\circ \leqslant \psi \leqslant 30^\circ$ yield a better collapse of the separation lines. Also, from hot-film measurements, detailed maps of skin-friction lines may be constructed as shown, for example, in figures 1(*b*) and 9(*c*), where it is possible to identify flow separations (i.e. skin-friction minima) further upstream of the slender body (Wetzel 1996).

To summarise, the power-law exponent $k$ defined by (4.3) can be used as a measure of separation rate to test the effect of the Reynolds number. In figures 7–9, the primary-separation rate $k_1$ and the secondary-separation rate $k_2$ are obtained by curve fitting all available data points for each Reynolds number $Re_L$. Plots of $k_1$ and $k_2$ in figure 10(*a*) show no strong dependence on the Reynolds number over the range $2.1 \times 10^6 \leqslant Re_L \leqslant 23 \times 10^6$, and so only horizontal lines of best fit $k_1 \simeq -0.190$ and $k_2 \simeq 0.045$ are included as a visual guide. A plot of the start time in figure 10(*b*) for the same Reynolds-number range shows $t_s^* \simeq 1.5$.

## 5. Envelope of flow separation

The results in figure 10 established that, for all the different body geometries considered on the axis of $\Theta$ as a function of $t^*$, the separation rates ($k_1$ and $k_2$) and the start time ($t_s^*$) are not dependent on the Reynolds number over the range $2.1 \times 10^6 \leqslant Re_L \leqslant 23 \times 10^6$. Figure 11 shows a plot of all the data points gathered from figures 7–9; the curves of best fit yield

$$\Theta_{B_1^-} = 151.2(t^*)^{-0.190}, \quad \Theta_{B_2^-} = 137.5(t^*)^{0.045}, \tag{5.1a,b}$$

with an r.m.s. difference of 6.3 % for the primary separation and 2.5 % for the secondary separation, where the curves start at $(t_s^*, \Theta_s) \simeq (1.5, 140^\circ)$. For the fitted curves, altering a least significant digit in each numerical coefficient in (5.1) changes the r.m.s. difference by no more than 1 %, and changes the model prediction of $\Theta_s$ by no more than $1^\circ$ at the start time $t_s^* = 1.5$.

https://doi.org/10.1017/jfm.2017.886 Published online by Cambridge University Press

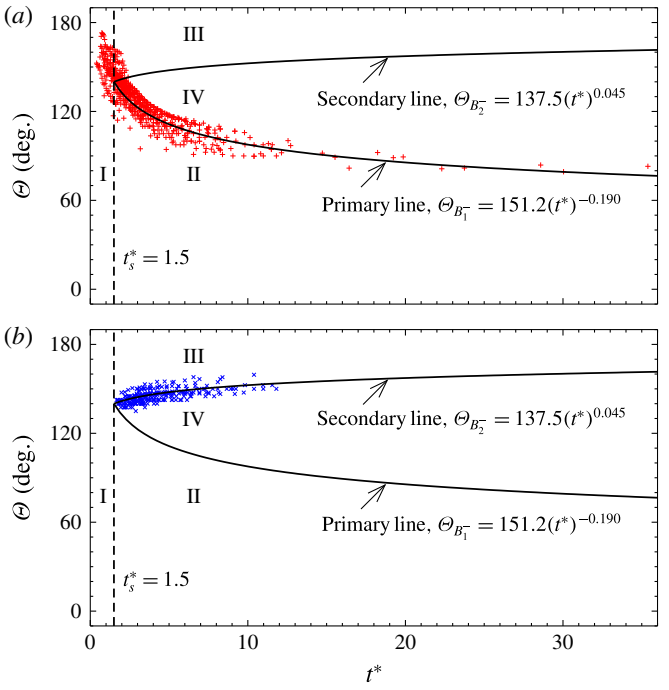


FIGURE 11. (Colour online) Power-law curve fits to all the data points from figures 7–9 for the body-length Reynolds number over the range $2.1 \times 10^6 \leqslant Re_L \leqslant 23 \times 10^6$: (*a*) primary-separation data, and (*b*) secondary-separation data. The locus chart constructed from (5.1) shows (I) the initial region, (II) the windward stream, (III) the leeward stream and (IV) the separation envelope.

In figure 11, the locus chart constructed from (5.1) summarises four regions of slender-body surface flow. Region 'I' in the range $t^* < t_s^*$ represents the initial development of separation over the slender body. Regions 'II' and 'III' in the range $t^* \geqslant t_s^*$ cover the windward and leeward streams, respectively. Region 'IV' defines the envelope of separation between the two streams, where the size of the separation $(\Theta_{B_2^-} - \Theta_{B_1^-})$ increases at a power-law rate of time $t^*$.

## 6. Conclusions

Surface-flow visualisation identifies the primary and secondary leeward-separation lines as key topological features on axisymmetric slender bodies at incidence. For the present collection of data, the incidence angles are between 6 and 35°. The windward side corresponds to the body azimuth angle $\Theta = 0°$ and the leeward side is at $\Theta = 180°$. The development of flow-separation lines is taken as a transient problem which relates the longitudinal distance $x$ to time $t^* = x \tan(\psi)/r(x)$, where $r(x)$ is the local body radius and $\psi$ is the incidence angle. The separation-line data fall on a power law $\Theta \sim (t^*)^k$. The separation rate $k$ does not depend on the body-length Reynolds number over the range $2.1 \times 10^6 \leqslant Re_L \leqslant 23 \times 10^6$, with $k_1 \simeq -0.190$ for the primary line and $k_2 \simeq 0.045$ for the secondary line. The power-law curve fits trace the separation lines to a characteristic start time $t_s^* \simeq 1.5$.

https://doi.org/10.1017/jfm.2017.886 Published online by Cambridge University Press

**Acknowledgements**

Thanks go to P. Jacquemin for operating the DST low-speed wind tunnel and to QinetiQ for manufacturing ancillary components for the slender bodies. This work acknowledges the helpful feedback from fellow DST colleagues and from the anonymous referees.

## REFERENCES

ALLEN, H. J. 1949 Estimation of the forces and moments acting on inclined bodies of revolution of high fineness ratio. *Tech. Rep.* NACA-RM-A9I26. National Advisory Committee for Aeronautics, Washington.

ASHOK, A., VAN BUREN, T. & SMITS, A. J. 2015 Asymmetries in the wake of a submarine model in pitch. *J. Fluid Mech.* **774**, 416–442.

CHESNAKAS, C. J. & SIMPSON, R. L. 1997 Detailed investigation of the three-dimensional separation about a 6:1 prolate spheroid. *AIAA J.* **35** (6), 990–999.

ERM, L. P. 2003 Calibration of the flow in the extended test section of the low-speed wind tunnel at DSTO. *Tech. Rep.* DSTO-TR-1384. Defence Science and Technology, Australia.

GROVES, N. C., HUANG, T. T. & CHANG, M. S. 1989 Geometric characteristics of DARPA SUBOFF models (DTRC model nos. 5470 and 5471). *Tech. Rep.* DTRC/SHD-1298-01. David Taylor Research Center, Bethesda.

JEANS, T. L. & HOLLOWAY, A. G. L. 2010 Flow-separation lines on axisymmetric bodies with tapered tails. *J. Aircraft* **47** (6), 2177–2183.

JEANS, T. L., WATT, G. D., GERBER, A. G., HOLLOWAY, A. G. L. & BAKER, C. R. 2009 High-resolution Reynolds-averaged Navier–Stokes flow predictions over axisymmetric bodies with tapered tails. *AIAA J.* **47** (1), 19–32.

JIANG, F., ANDERSSON, H. I., GALLARDO, J. P. & OKULOV, V. L. 2016 On the peculiar structure of a helical wake vortex behind an inclined prolate spheroid. *J. Fluid Mech.* **801**, 1–12.

LEE, S.-K. 2015 Topology model of the flow around a submarine hull form. *Tech. Rep.* DST-Group-TR-3177. Defence Science and Technology, Australia.

MACKAY, M. 2003 The standard submarine model: a survey of static hydrodynamic experiments and semiempirical predictions. *Tech. Rep.* TR-2003-079. Defence Research and Development Canada.

SARPKAYA, T. 1966 Separated flow about lifting bodies and impulsive flow about cylinders. *AIAA J.* **4** (3), 414–420.

SCHINDEL, L. H. 1969 Effects of vortex separation on the lift distribution on bodies of elliptic cross section. *J. Aircraft* **6** (6), 537–543.

TOBAK, M. & PEAKE, D. J. 1982 Topology of three-dimensional separated flows. *Annu. Rev. Fluid Mech.* **14**, 61–85.

VAN RANDWIJCK, E. F. & FELDMAN, J. P. 2000 Results of experiments with a segmented model to investigate the distribution of the hydrodynamics forces and moments on a streamlined body of revolution at an angle of attack or with a pitching angular velocity. *Tech. Rep.* NSWCCD-50-TR-2000/008. Naval Surface Warfare Center Carderock Division.

WANG, K. C. 1972 Separation patterns of boundary layer over an inclined body of revolution. *AIAA J.* **10** (8), 1044–1050.

WETZEL, T. G. 1996 Unsteady flow over a 6:1 prolate spheroid. PhD thesis, Department of Aerospace and Ocean Engineering, Virginia Polytechnic Institute and State University, Blacksburg, Virginia.

WETZEL, T. G., SIMPSON, R. L. & CHESNAKAS, C. J. 1998 Measurement of three-dimensional crossflow separation. *AIAA J.* **36** (4), 557–564.

https://doi.org/10.1017/jfm.2017.886 Published online by Cambridge University Press